Physics Faculty Publications   Physics Department

1-1-2008

"Polarized structure function σLT' for 1H(e→,e'K+)Λ in the nucleon resonance region

R. Nasseripour

Angela Biselli
Fairfield University, abiselli@fairfield.edu

CLAS Collaboration

Peer Reviewed

Repository Citation

Published Citation

Polarized structure function $\sigma_{LT'}$ for $^1H(\vec{e}, e'K^+)\Lambda$ in the nucleon resonance region

R. Nasseripour,[1,2] B. A. Raue,[1] D. S. Carman,[3] P. Ambrozewicz,[1] M. J. Amaryan,[32] E. Anciant,[10] M. Anghinolfi,[21] B. Asavapibhop,[27] G. Asryan,[41] G. Audit,[10] T. Auger,[10] H. Avakian,[3] H. Bagdasaryan,[32] N. Baillie,[40] J. P. Ball,[5] N. A. Baltzell,[2] S. Barrow,[15] M. Battaglieri,[21] K. Beard,[24] I. Bedlinskiy,[23] M. Bektasoglu,[32] M. Bellis,[8] N. Benmouna,[17] B. L. Berman,[17] A. S. Biselli,[14] L. Blaszczyk,[15] B. E. Bonner,[35] S. Bouchigny,[3,22] S. Boiarinov,[3] R. Bradford,[8] D. Branford,[13] W. J. Briscoe,[17] W. K. Brooks,[3] V. D. Burkert,[3] C. Butuceanu,[40] J. R. Calarco,[29] S. L. Careccia,[32] L. Casey,[9] C. Cetina,[17] S. Chen,[15] L. Cheng,[9] P. L. Cole,[19] P. Collins,[5] P. Coltharp,[15] D. Cords,[3,*] P. Corvisiero,[21] D. Crabb,[39] V. Crede,[15] D. Dale,[19] N. Dashyan,[41] R. De Masi,[10] R. De Vita,[21] E. De Sanctis,[20] P. V. Degtyarenko,[3] L. Dennis,[15] A. Deur,[3] K. S. Dhuga,[17] R. Dickson,[8] C. Djalali,[2] G. E. Dodge,[32] D. Doughty,[3,11] P. Dragovitsch,[15] M. Dugger,[5] S. Dytman,[33] O. P. Dzyubak,[2] H. Egiyan,[29] K. S. Egiyan,[41,*] L. El Fassi,[4] L. Elouadrhiri,[3,11] P. Eugenio,[15] R. Fatemi,[39] G. Fedotov,[28] G. Feldman,[17] R. J. Feuerbach,[8] T. A. Forest,[19] A. Fradi,[22] H. Funsten,[40,*] M. Garçon,[10] G. Gavalian,[29,32] N. Gevorgyan,[41] G. P. Gilfoyle,[36] K. L. Giovanetti,[24] P. Girard,[2] F. X. Girod,[10] J. T. Goetz,[6] R. W. Gothe,[2] K. A. Griffioen,[40] M. Guidal,[22] M. Guillo,[2] N. Guler,[32] L. Guo,[3] V. Gyurjyan,[3] K. Hafidi,[4] H. Hakobyan,[41] C. Hanretty,[15] J. Hardie,[3,11] D. Heddle,[3,11] F. W. Hersman,[29] K. Hicks,[31] I. Hleiqawi,[31] M. Holtrop,[29] J. Hu,[34] C. E. Hyde-Wright,[32] Y. Ilieva,[17] D. G. Ireland,[18] B. S. Ishkhanov,[28] E. L. Isupov,[28] M. M. Ito,[3] D. Jenkins,[38] H. S. Jo,[22] J. R. Johnstone,[18] K. Joo,[12,39] H. G. Juengst,[32] N. Kalantarians,[32] J. D. Kellie,[18] M. Khandaker,[30] K. Y. Kim,[33] K. Kim,[25] W. Kim,[25] A. Klein,[32] F. J. Klein,[9] M. Kossov,[23] Z. Krahn,[8] L. H. Kramer,[1,3] V. Kubarovsky,[3,34] J. Kuhn,[8] S. E. Kuhn,[32] S. V. Kuleshov,[23] V. Kuznetsov,[25] J. Lachniet,[32] J. M. Laget,[3,10] J. Langheinrich,[2] D. Lawrence,[3] K. Livingston,[18] H. Y. Lu,[2] K. Lukashin,[9] M. MacCormick,[22] J. J. Manak,[3] N. Markov,[12] P. Mattione,[35] S. McAleer,[15] B. McKinnon,[18] J. W. C. McNabb,[8] B. A. Mecking,[3] M. D. Mestayer,[3] C. A. Meyer,[8] T. Mibe,[31] K. Mikhailov,[23] R. Minehart,[39] M. Mirazita,[20] R. Miskimen,[27] V. Mokeev,[3,28] B. Moreno,[22] K. Moriya,[8] S. A. Morrow,[10,22] M. Moteabbed,[1] J. Mueller,[33] E. Munevar,[17] G. S. Mutchler,[35] P. Nadel-Turonski,[17] S. Niccolai,[22] G. Niculescu,[24] I. Niculescu,[24] B. B. Niczyporuk,[3] M. R. Niroula,[32] R. A. Niyazov,[3,32] M. Nozar,[3] M. Osipenko,[21,28] A. I. Ostrovidov,[15] K. Park,[2] E. Pasyuk,[5] C. Paterson,[18] S. Anefalos Pereira,[20] G. Peterson,[27] S. A. Philips,[17] J. Pierce,[39] N. Pivnyuk,[23] D. Pocanic,[39] O. Pogorelko,[23] S. Pozdniakov,[23] B. M. Preedom,[2] J. W. Price,[7] S. Procureur,[10] Y. Prok,[11] D. Protopopescu,[18] L. M. Qin,[32] G. Riccardi,[15] G. Ricco,[21] M. Ripani,[21] B. G. Ritchie,[5] G. Rosner,[18] P. Rossi,[20] P. D. Rubin,[36] F. Sabatié,[10,32] J. Salamanca,[19] C. Salgado,[30] J. P. Santoro,[9] V. Sapunenko,[3,21] D. Sayre,[31] R. A. Schumacher,[8] V. S. Serov,[23] A. Shafi,[17] Y. G. Sharabian,[3] D. Sharov,[28] N. V. Shvedunov,[28] S. Simionatto,[17] A. V. Skabelin,[26] E. S. Smith,[3] L. C. Smith,[39] D. I. Sober,[9] D. Sokhan,[13] A. Stavinsky,[23] S. S. Stepanyan,[25] S. Stepanyan,[3] B. E. Stokes,[15] P. Stoler,[34] I. I. Strakovsky,[17] S. Strauch,[2] M. Taiuti,[21] S. Taylor,[3] D. J. Tedeschi,[2] R. Thompson,[33] A. Tkabladze,[17] S. Tkachenko,[32] M. Ungaro,[12] M. F. Vineyard,[37] A. V. Vlassov,[23] K. Wang,[39] D. P. Watts,[18] L. B. Weinstein,[32] D. P. Weygand,[3] M. Williams,[8] E. Wolin,[3] M. H. Wood,[2] A. Yegneswaran,[3] J. Yun,[32] L. Zana,[29] J. Zhang,[32] B. Zhao,[12] and Z. W. Zhao[2]

(CLAS Collaboration)

[1]*Florida International University, Miami, Florida 33199, USA*
[2]*University of South Carolina, Columbia, South Carolina 29208, USA*
[3]*Thomas Jefferson National Accelerator Facility, Newport News, Virginia 23606, USA*
[4]*Argonne National Laboratory, Argonne, Illinois 60439, USA*
[5]*Arizona State University, Tempe, Arizona 85287-1504, USA*
[6]*University of California at Los Angeles, Los Angeles, California 90095-1547, USA*
[7]*California State University Dominguez Hills, Carson, California 90747, USA*
[8]*Carnegie Mellon University, Pittsburgh, Pennsylvania 15213, USA*
[9]*Catholic University of America, Washington, DC 20064, USA*
[10]*CEA-Saclay, Service de Physique Nucléaire, F-91191 Gif-sur-Yvette, France*
[11]*Christopher Newport University, Newport News, Virginia 23606, USA*
[12]*University of Connecticut, Storrs, Connecticut 06269, USA*
[13]*Edinburgh University, Edinburgh EH9 3JZ, United Kingdom*
[14]*Fairfield University, Fairfield, Connecticut 06824, USA*
[15]*Florida State University, Tallahassee, Florida 32306, USA*
[16]*Physikalisches Institut der Universitaet Giessen, D-35392 Giessen, Germany*
[17]*George Washington University, Washington, DC 20052, USA*
[18]*University of Glasgow, Glasgow G12 8QQ, United Kingdom*
[19]*Idaho State University, Pocatello, Idaho 83209, USA*
[20]*INFN, Laboratori Nazionali di Frascati, I-00044 Frascati, Italy*
[21]*INFN, Sezione di Genova, I-16146 Genova, Italy*
[22]*Institut de Physique Nucleaire ORSAY, Orsay, France*
[23]*Institute of Theoretical and Experimental Physics, RU-117259 Moscow, Russia*
[24]*James Madison University, Harrisonburg, Virginia 22807, USA*
[25]*Kyungpook National University, Daegu 702-701, Republic of Korea*

^{26}*Massachusetts Institute of Technology, Cambridge, Massachusetts 02139-4307, USA*

^{27}*University of Massachusetts, Amherst, Massachusetts 01003, USA*

^{28}*Moscow State University, General Nuclear Physics Institute, RU-119899 Moscow, Russia*

^{29}*University of New Hampshire, Durham, New Hampshire 03824-3568, USA*

^{30}*Norfolk State University, Norfolk, Virginia 23504, USA*

^{31}*Ohio University, Athens, Ohio 45701, USA*

^{32}*Old Dominion University, Norfolk, Virginia 23529, USA*

^{33}*University of Pittsburgh, Pittsburgh, Pennsylvania 15260, USA*

^{34}*Rensselaer Polytechnic Institute, Troy, New York 12180-3590, USA*

^{35}*Rice University, Houston, Texas 77005-1892, USA*

^{36}*University of Richmond, Richmond, Virginia 23173, USA*

^{37}*Union College, Schenectady, New York 12308, USA*

^{38}*Virginia Polytechnic Institute and State University, Blacksburg, Virginia 24061-0435, USA*

^{39}*University of Virginia, Charlottesville, Virginia 22901, USA*

^{40}*College of William and Mary, Williamsburg, Virginia 23187-8795, USA*

^{41}*Yerevan Physics Institute, 375036 Yerevan, Armenia*

The first measurements of the polarized structure function $\sigma_{LT'}$ for the reaction $^1\mathrm{H}(\vec{e}, e'K^+)\Lambda$ in the nucleon resonance region are reported. Measurements are included from threshold up to $W = 2.05$ GeV for central values of Q^2 of 0.65 and 1.00 GeV^2, and nearly the entire kaon center-of-mass angular range. $\sigma_{LT'}$ is the imaginary part of the longitudinal-transverse response and is expected to be sensitive to interferences between competing intermediate s-channel resonances, as well as resonant and nonresonant processes. The results for $\sigma_{LT'}$ are comparable in magnitude to previously reported results from CLAS for σ_{LT}, the real part of the same response. An intriguing sign change in $\sigma_{LT'}$ is observed in the high Q^2 data at $W \approx 1.9$ GeV. Comparisons to several existing model predictions are shown.

I. INTRODUCTION

The study of the electromagnetic production of strange quarks in the resonance region plays an important role in understanding the strong interaction. The $^1\mathrm{H}(\vec{e}, e'K^+)\Lambda$ reaction involves the production of the strange particles $\Lambda(uds)$ and $K^+(u\bar{s})$ in the final state via strange quark-pair ($s\bar{s}$) creation. The fundamental theory for the description of the dynamics of quarks and gluons is known as quantum chromodynamics (QCD). However, while numerical approaches to QCD in the medium-energy regime do exist, neither perturbative QCD nor lattice QCD can presently predict the hadron properties seen in this type of reaction. In the nonperturbative regime of nucleon resonance physics, the consequence is that the interpretation of dynamical hadronic processes still hinges to a significant degree on models containing some phenomenological ingredients. Various quark models (see, for example, Refs. [1–4]) predict a large number of nonstrange baryons that can decay into a strange baryon and a strange meson, as well as $N\pi/N\pi\pi$ final states. While many of these excited states have been observed in pion production data, a large number are "missing." The higher threshold for $K^+\Lambda$ final states kinematically favors production of the missing resonances with masses near 2 GeV. Studies of different final states, such as the associated production of strangeness, can provide complementary information on the contributing amplitudes.

In the absence of direct QCD predictions, effective models must be employed. Utilizing these models by means of fitting them to the available experimental data—cross sections and polarization observables—or comparing the data to the model predictions, can provide information on the reaction dynamics. In addition, these comparisons can provide important qualitative and quantitative information on the contributing resonant and nonresonant terms in the s, t, and u reaction channels (see Fig. 1). The development of these theoretical models has been highly based on the availability of the experimental data. Precise measurements of cross sections and polarization observables are crucial to the refinement of these models and the search for missing resonances.

In this paper, we report the first-ever measurements of the longitudinal-transverse polarized structure function $\sigma_{LT'}$ for the $^1\mathrm{H}(\vec{e}, e'K^+)\Lambda$ reaction in the resonance region, using the CEBAF large acceptance spectrometer (CLAS) in Hall B of the Thomas Jefferson National Accelerator Facility (JLab). This observable provides complementary information to the σ_{LT} structure function reported in Ref. [5], as will be discussed. Thus, these new data provide another constraint on model parameters and, therefore, provide additional important information in understanding the process of electromagnetic production of strangeness.

There is a growing body of high-quality data on the electromagnetic production of strange hadrons. Recently published data using electron beams exist on the separation of the longitudinal and transverse structure functions, σ_L and σ_T, from Hall C of JLab for both $K^+\Lambda$ and $K^+\Sigma^0$ final states
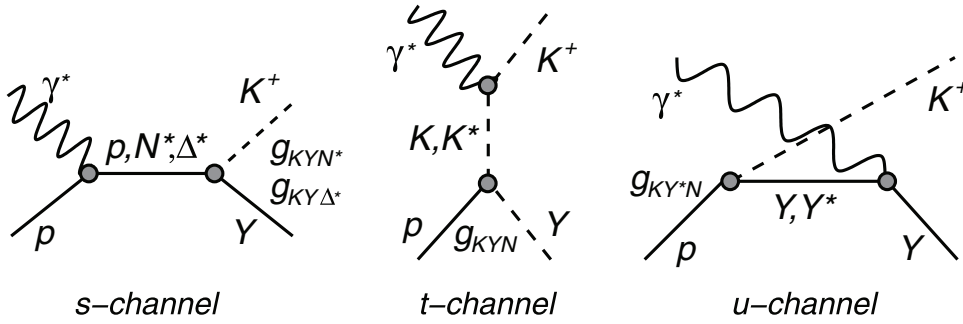
FIG. 1. Feynman diagrams representing s-channel nucleon (p, N^*, Δ^*) exchange, t-channel kaon (K, K^*) exchange, and u-channel hyperon (Y, Y^*) exchange that contribute to the reaction models. The vertex labels g_{MBB} represent the strong coupling constants.

at an invariant energy $W = 1.84$ GeV, for momentum transfers Q^2 up to 2.0 GeV^2, at a kaon center-of-mass scattering angle of $\theta_K^* = 0°$ [6,7]. The CLAS Collaboration has recently produced results in which unpolarized cross sections and interference structure functions (σ_{TT} and σ_{LT}) were measured for $K^+\Lambda$ and $K^+\Sigma^0$ final states over a wide kinematic range with Q^2 up to 2.6 GeV^2, W up to 2.4 GeV, and nearly complete angular coverage in the center-of-mass frame [5]. These results include the first-ever separation of σ_L and σ_T at angles other than $\theta_K^* = 0°$. The same data set has been analyzed to extract the polarization transfer from the virtual photon to the produced Λ hyperon [8] and to extract the ratio of σ_L/σ_T at $\theta_K^* = 0°$ for the $K^+\Lambda$ final state [9]. Older electroproduction data from various laboratories also exist [10–14], but with much larger uncertainties and much smaller kinematic coverage.

Complementary data from photoproduction are also available. The SAPHIR Collaboration has published total and differential cross section data for the photoproduction of $K^+\Lambda$ and $K^+\Sigma^0$ final states with photon energies up to 2 GeV [15,16]. CLAS has provided extensive differential cross sections [17,18], along with recoil [17] and transferred polarization [19] data for the same final states in similar kinematics. Finally, the LEPS Collaboration has measured differential cross sections and polarized beam asymmetries with a linearly polarized photon beam for energies up to 2.4 GeV at forward angles [20,21].

The SAPHIR cross section data show an interesting resonance-like structure in the $K^+\Lambda$ final state around $W = 1.9$ GeV. A similar structure has been seen in the unpolarized electroproduction cross section data [5], as well as in the photoproduction measurements of CLAS [17,18]. Within the isobar model of Mart and Bennhold [22,23], that structure was interpreted as a $D_{13}(1895)$ resonance, which had been predicted by several quark models (e.g., in Ref. [4]), but not well established. However, the isobar model of Saghai [24] found that the cross section data could be satisfactorily described without the need for including any new s-channel resonances by including higher-spin u-channel exchange terms. The need to include the missing $D_{13}(1895)$ state, however, was supported by the new Regge plus resonance model from Ghent [25] that compared their model to a broad set of cross section and polarization observables from the available photo- and electroproduction data. Therefore, more measurements, including polarization data, are needed to further develop the theoretical models to interpret the structures observed in the cross sections.

The organization of this paper includes an overview of the relevant formalism in Sec. II, a description of the theoretical models used to compare against the data in Sec. III, details on the experiment and data analysis in Sec. IV, and a presentation and discussion of the results in Sec. V. The conclusions are given in Sec. VI.

II. FORMALISM

A schematic diagram of $K^+\Lambda$ electroproduction off a fixed hydrogen target is shown in Fig. 2. The angle between the incident and scattered electron is θ_e, while the angle between the electron scattering plane and hadron production plane is defined as ϕ. In the one-photon exchange approximation, the interaction between the incident electron beam and the target proton is mediated by a virtual photon, γ^*. The virtual photon four-momentum is obtained from the difference between the four-momenta of the incident, $e = (E, \mathbf{p}_e)$, and scattered electrons, $e' = (E', \mathbf{p}'_e)$, as

$$q = e - e' = (\nu, \mathbf{q}). \tag{1}$$

The four-momentum transfer squared Q^2 is an invariant quantity defined as

$$Q^2 = -q^2 = -(\nu^2 - \mathbf{q}^2) = 4EE' \sin^2(\theta_{e'}/2), \tag{2}$$

where $\nu = E - E'$ is the energy transfer and $\theta_{e'}$ is the electron scattering angle in the laboratory frame. The invariant mass W of the intermediate hadronic state is defined as

$$W^2 = s = M^2 + 2M\nu - Q^2, \tag{3}$$

where M is the mass of the proton target.

Following the notation of Refs. [26,27], the differential cross section for KY electroproduction in the center-of-mass
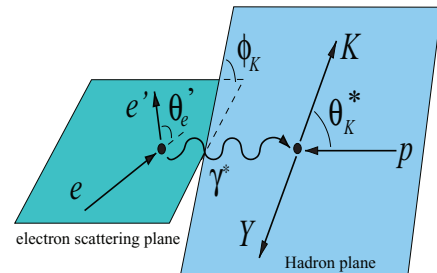

FIG. 2. (Color online) Kinematic diagram for kaon-hyperon (KY) electroproduction.

frame is given by

$$\frac{d\sigma}{dE' d\Omega_{e'} d\Omega_K^*} = \Gamma \frac{d\sigma}{d\Omega_K^*}, \tag{4}$$

where Γ is the virtual photon flux given by

$$\Gamma = \frac{\alpha}{4\pi^2} \frac{E'}{E} \frac{W^2 - M^2}{M} \frac{1}{Q^2} \left(\frac{1}{1-\epsilon}\right). \tag{5}$$

Here $\frac{d\sigma}{d\Omega_K^*}$ is the virtual photon cross section and ϵ is the virtual photon transverse polarization component defined as

$$\epsilon = \left[1 + 2\left(1 + \frac{\nu^2}{Q^2}\right) \tan^2 \frac{\theta_{e'}}{2}\right]^{-1}. \tag{6}$$

The cross section for the electromagnetic interaction of a relativistic electron beam with a hadron target is obtained by calculating the transition probability of the process [28]. The cross section can be written in the form of a contraction between leptonic and hadronic tensors that separately contain the electron and hadron variables. In general, the lepton tensor can be written in terms of a density matrix of virtual photon polarization that contains a symmetric helicity-independent part and an antisymmetric helicity-dependent part. The antisymmetric part contributes to the cross section only when the hadron tensor also contains an antisymmetric part. This is the case when scattering a polarized electron off of an unpolarized target with the detection of the final state hadron in coincidence with the scattered electron. The antisymmetric part vanishes for the case of unpolarized electrons.

For a polarized electron beam with helicity h and no target or recoil polarizations, the virtual photon cross section can be written as

$$\frac{d\sigma}{d\Omega_K^*} = \sigma_T + \epsilon\sigma_L + \epsilon\sigma_{TT} \cos 2\phi + \sqrt{\epsilon(1+\epsilon)}\sigma_{LT} \cos\phi$$
$$+ h\sqrt{\epsilon(1-\epsilon)}\sigma_{LT'} \sin\phi, \tag{7}$$

where σ_i are the structure functions that measure the response of the hadronic system and $i = T, L, LT, TT$, and LT' represent the transverse, longitudinal, and interference structure functions. The structure functions are, in general, functions of Q^2, W, and θ_K^* only. Note that the convention employed here for the differential cross section is not used by all authors.[1]

For the case of an unpolarized electron beam, Eq. (7) reduces to the unpolarized cross section σ_0, i.e.,

$$\frac{d\sigma}{d\Omega_K^*} \equiv \sigma_0 = \sigma_T + \epsilon\sigma_L + \epsilon\sigma_{TT} \cos 2\phi$$
$$+ \sqrt{\epsilon(1+\epsilon)}\sigma_{LT} \cos\phi. \tag{8}$$

The electron polarization therefore produces a fifth structure function that is related to the beam helicity asymmetry via

$$A_{LT'} = \frac{\left(\frac{d\sigma}{d\Omega_K^*}\right)^+ - \left(\frac{d\sigma}{d\Omega_K^*}\right)^-}{\left(\frac{d\sigma}{d\Omega_K^*}\right)^+ + \left(\frac{d\sigma}{d\Omega_K^*}\right)^-} = \frac{\sqrt{\epsilon(1-\epsilon)}\sigma_{LT'} \sin\phi}{\sigma_0}. \tag{9}$$

The $\pm$ superscripts on $\frac{d\sigma}{d\Omega_K^*}$ correspond to the electron helicity states of $h = \pm 1$. Clearly, $\sigma_{LT'}$ can only be observed when the outgoing hadron is detected out of the electron scattering plane ($\phi \neq 0$) and can be separated by flipping the electron helicity.

The structure functions are defined in terms of the independent elements of the hadron tensor in the center-of-mass frame, $W'_{\lambda\lambda'}$ [28], as

$$\sigma_L \propto W'_{00},$$
$$\sigma_T \propto (W'_{11} + W'_{-1-1}),$$
$$\sigma_{TT} \propto W'_{1-1}, \tag{10}$$
$$\sigma_{LT} \propto \text{Re} (W'_{01} - W'_{0-1}),$$
$$\sigma_{LT'} \propto \text{Im} (W'_{01} - W'_{0-1}),$$

where the indices $\lambda, \lambda' = 0$ for the longitudinal component and $\lambda, \lambda' = \pm 1$ for the two transverse components. In contrast to the case of real photons, where there is only the purely transverse response, virtual photons allow longitudinal, transverse-transverse, and longitudinal-transverse interference terms to occur.

The polarized structure function $\sigma_{LT'}$ is intrinsically different from the four structure functions of the unpolarized cross section. As seen by Eqs. (10), this term is generated by the imaginary part of terms involving the interference between longitudinal and transverse components of the hadronic and leptonic currents. This is in contrast to σ_{LT}, which is generated by the real part of the same interference. $\sigma_{LT'}$ is nonvanishing only if the hadronic tensor is antisymmetric, which will occur in the presence of final state interaction (FSI) (or rescattering) effects, interferences between multiple resonances, interferences between resonant and nonresonant processes, or even between nonresonant processes alone. On the other hand, $\sigma_{LT'}$ could be nonzero even when σ_{LT} (which is not expected to be sensitive to FSI effects [28]) is zero. It provides a means of measuring the contributions of small resonance channels that are often too weak to be observed directly in the unpolarized cross sections. Furthermore, when the reaction proceeds through a channel in which a single amplitude dominates, the longitudinal-transverse response will be real and $\sigma_{LT'}$ vanishes. Both σ_{LT} and $\sigma_{LT'}$ are necessary to fully unravel the longitudinal-transverse response of the $K^+\Lambda$ electroproduction reaction.

III. THEORETICAL MODELS

With the recently available data from the photo- and electro-production of KY final states from CLAS and elsewhere, there have been renewed efforts in the development of theoretical models. The majority of these are single-channel models that represent tree-level calculations, where the amplitude is constructed from the lowest-order Feynman diagrams (see

---

[1]Some authors use a prefactor for the σ_L term of ϵ_L, for the $\sigma_{LT}(\sigma_{LT'})$ term of $\sqrt{2\epsilon_L(1+\epsilon)}(\sqrt{2\epsilon_L(1-\epsilon)})$ instead, where $\epsilon_L = \epsilon Q^2/\nu^2_{\text{c.m.}}$ parametrizes the longitudinal polarization of the virtual photon. Some also take a $\cos\theta_K^* (\sin\theta_K^*)$ term out of the definition of $\sigma_{LT}(\sigma_{LT'})$ and a $\cos 2\theta_K^*$ term out of the definition of σ_{TT} (see, e.g., Ref. [27]).

Ref. [25] and references therein). More recent work has moved beyond the single-channel approach with the development of coupled-channels models [29–32] or by fitting simultaneously to multiple, independent reaction channels [33,34]. However, as a combined coupled-channels analysis of the photo- and electroproduction reactions is not yet available, a tree-level approach currently represents the best possibility of studying both reactions within the same framework. While most of the recent theoretical analyses have focused solely on the available photoproduction data, it has been shown that electroproduction observables can yield important complementary insights to improve and constrain theory [25].

At the medium energies used in this experiment, perturbative QCD is not capable of providing any predictions for the differential cross sections or structure functions for kaon electroproduction. In this work, the results are compared against three different model approaches. The first is a traditional hadrodynamic (resonance) model, the second is based on a Reggeon-exchange model, and the third is a hybrid Regge plus resonance approach.

In the hadrodynamic model approach, the strong interaction is modeled by an effective Lagrangian, which is constructed from tree-level Born and extended Born terms for intermediate states exchanged in the $s, t,$ and u reaction channels (see Fig. 1). Each resonance has its own strong coupling constants and strong decay widths. A complete description of the physics processes requires taking into account all possible channels that could couple to the initial and final state measured, but the advantages of the tree-level approach include the ability to limit complexity and to identify the dominant trends. In the one-channel, tree-level approach, several dozen parameters must be fixed by fitting to the data, since they are poorly known and not constrained from other sources.

The hadrodynamic model employed in this work was developed by Mart and Bennhold [23,35] (referred to here as MB). In this model, the coupling strengths have been determined mainly by fits to existing $\gamma p \rightarrow K^+ Y$ data (with some older electroproduction data included), leaving the coupling constants as free parameters [constrained loosely by SU(3) symmetry requirements]. It employs phenomenological form factors to account for the extension of the point-like interactions at the hadronic vertices. This model has been compared against the existing photoproduction data from SAPHIR [15,16] and CLAS [17,18], and provides a fair description of those results. The model parameters are not based on fits to any CLAS data. The specific resonances included in this model are the $S_{11}(1650)$, $P_{11}(1710)$, $P_{13}(1720)$, and $D_{13}(1895)$ N^* states in the s channel, and the $K^*(892)$ and $K_1^*(1270)$ in the t channel.

The data are also compared with the Reggeon-exchange model from Guidal, Laget, and Vanderhaeghen [36] (referred to here as GLV). This calculation includes no baryon resonance terms at all. Instead, it is based only on gauge-invariant t-channel K and K^* Regge-trajectory exchange. It therefore provides a complementary basis for studying the underlying dynamics of strangeness production. It is important to note that the Regge approach has far fewer parameters than the hadrodynamic models. These include the K and K^* form factors (assumed to be of a monopole form) and the coupling

constants g_{KYN} and g_{K^*YN} (taken from photoproduction studies).

The GLV model was fit to higher energy photoproduction data, where there is little doubt of the dominance of these kaon exchanges, and extrapolated down to JLab energies. An important feature of this model is the way gauge invariance is achieved for the K and K^* t-channel exchanges by Reggeizing the s-channel nucleon pole contribution in the same manner as the t-channel diagrams [36]. Because of gauge invariance, the t-channel exchanges and s-channel nucleon pole terms are inseparable and are treated on the same footing. They are Reggeized in the same way and multiplied by the same electromagnetic form factor. No counter terms need to be introduced to restore gauge invariance as is done in the hadrodynamic approach.

The final model included in this work was developed by the University of Ghent group [25] and is based on a tree-level effective field model for Λ and Σ^0 photoproduction from the proton. It differs from traditional isobar approaches in its description of the nonresonant diagrams, which involve the exchange of K and K^* Regge trajectories. A selection of s-channel resonances are then added to this background. This "Regge plus resonance" (referred to here as RPR) approach has the advantage that the background diagrams contain only a few parameters that are constrained by high-energy data where the t-channel processes dominate. Furthermore, the use of Regge propagators eliminates the need to introduce strong form factors in the background terms, thus avoiding the gauge-invariance issues associated with the traditional effective Lagrangian models. In addition to the kaonic trajectories to model the t-channel background, the RPR model includes the s-channel resonances $S_{11}(1650)$, $P_{11}(1710)$, $P_{13}(1720)$, and $P_{13}(1900)$. Apart from these, the model includes either a $D_{13}(1900)$ or $P_{11}(1900)$ state in the $K^+\Lambda$ channel. In detailed comparisons with the separated structure functions [5] and beam-recoil transferred polarization data from CLAS [8], only the $D_{13}(1900)$ assumption could be reconciled with the data, whereas the $P_{11}(1900)$ option could clearly be rejected [25]. Note that the CLAS electroproduction data strongly suggest a reaction mechanism for $K^+\Lambda$ dominated by t-channel exchange due to the strong forward peaking of the cross section. However, there are obvious discrepancies with the Regge predictions, which are based solely on t-channel exchanges. This is indicative of s-channel contributions in the $K^+\Lambda$ production dynamics [5].

IV. EXPERIMENT AND DATA ANALYSIS

A. Experimental apparatus

The data included in this work were taken in 1999, using the high duty factor electron beam at JLab and the CEBAF large acceptance spectrometer (CLAS) [37] in Hall B. A longitudinally polarized 2.567 GeV electron beam with a current of 5 nA was incident upon a 5-cm-long liquid-hydrogen target with a density of 0.073 g/cm^3, resulting in a luminosity of $\sim 10^{34}$ cm^{-2} s^{-1}. The electron beam polarization was measured regularly throughout the experiment with a coincidence Møller

polarimeter [37]. The average beam polarization was measured to be 67.0±1.5%.

CLAS is a large acceptance spectrometer used to detect multiparticle final states. Six superconducting coils generate a toroidal magnetic field around the target with azimuthal symmetry about the beam axis. The coils divide CLAS into six sectors, each functioning as an independent magnetic spectrometer. Each sector is instrumented with drift chambers (DCs) to determine charged-particle trajectories [38], scintillator counters (SCs) for time-of-flight measurements [39], and, in the forward region, gas-filled threshold Cherenkov counters (CCs) for electron/pion separation up to 2.5 GeV [40] and electromagnetic calorimeters (ECs) to identify and measure the energy of electrons and high-energy neutral particles, as well as to provide electron/pion separation above 2.5 GeV [41]. The trigger for the data acquisition readout of CLAS was a coincidence between the CC and EC in a given sector, which selected the electron candidates. For the data sets used in the present work, the total number of triggers collected was 530 M and 370 M for the two torus current settings of 1500 and 2250 A, respectively. These two data sets were combined together for the present analysis.

B. Data binning

The data were binned in a four-dimensional space of the independent kinematic variables Q^2, W, $\cos \theta_K^*$, and ϕ. Table I gives the binning in the variables Q^2, W, and $\cos \theta_K^*$, while ϕ was binned in eight, equal-sized bins running from $-180°$ to $180°$. A small fraction ($<5\%$) of the ϕ bins were excluded from this analysis because of their low acceptance in CLAS. A point was rejected if its acceptance was less than 2.0% (absolute) or less than 10% of the average acceptance over all bins at the same Q^2, W, and $\cos \theta_K^*$. These tend to be the bins adjacent to $\phi = 0°$ where the asymmetry is small because of the $\sin \phi$ dependence seen in Eq. (9), and therefore their absence has little effect on the extraction of $\sigma_{LT'}$.

C. Particle identification

The ${}^1\mathrm{H}(\vec{e}, e'K^+)\Lambda$ reaction was isolated by detecting the scattered electron e' and kaon K^+ with CLAS and

reconstructing the hyperon via the missing-mass technique. Electrons were identified by producing an electromagnetic shower in the EC accompanied by a signal in the CC. The electron energy deposited in the EC for all electron candidates was required to be consistent with the momentum measured by the track reconstruction in the DC. Electron and pion separation was also made by distinguishing between their different interaction modes in the EC. The start time of the interaction was then obtained by calculating the difference between the time measured by the SC and the flight time measured by the DC. This measured start time was combined with the hadron momentum and the path length measured by the DC to determine the hadron mass.

Corrections to the electron and kaon momenta were devised to correct for reconstruction inaccuracies. These arise from the relative misalignments of the drift chambers in the CLAS magnetic field, as well as from uncertainties in the magnetic field map employed during charged track reconstructions. These corrections were typically less than 1%.

Because of the small fraction of events containing kaons in the CLAS data, a preselection of kaon events based on preliminary particle identification was made. Here the kaon candidates were selected by choosing positively charged particles with a reconstructed mass between 0.3 and 0.7 GeV. Because the relative momentum resolution of CLAS becomes poorer with increasing momentum, a momentum-dependent mass cut was used. Figure 3(a) shows the reconstructed hadron mass as a function of momentum along with the cut used. Figure 3(b) shows the projected hadron mass distribution for all hadrons that passed the preselection criterion.

Hyperons are identified by using the four-momenta of the electron beam, scattered electron, and the K^+ candidate. The missing-mass distribution contains a background that includes a continuum beneath the hyperons from multiparticle final states with misidentified pions and protons, as well as events from ep elastic scattering (protons misidentified as kaons) and events from π^+n final states (pions misidentified as kaons). The elastic events are kinematically correlated and show up clearly in plots of θ_K^* versus missing mass and θ_K versus Q^2 [Figs. 4(a) and 4(b), respectively]. A cut on the elastic band in the θ_K (laboratory angle) versus Q^2 plot removes them without a significant loss of hyperon yield. The π^+n events

TABLE I. Ranges and centers of the kinematic bins used in this analysis. Note that the Q^2 bin from 0.8 to 1.3 GeV^2 was bin-centered to the value of 1.00 GeV^2 in this work (see Sec. IV H).

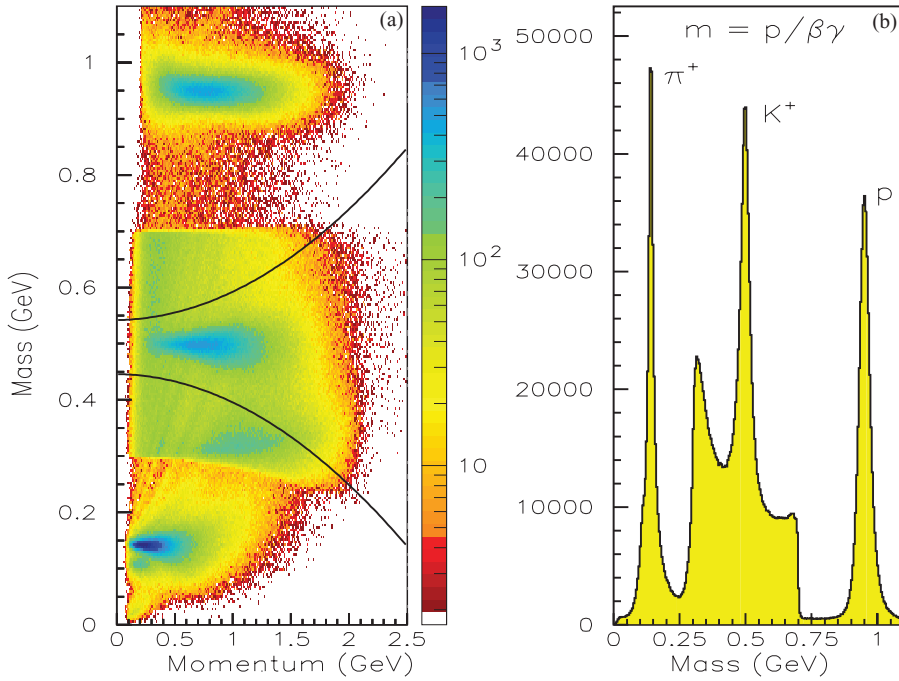| Q^2 (GeV^2)		W (GeV)		$\cos \theta_K^*$	
Range	Bin center	Range	Bin center	Range	Bin center
0.50 to 0.80	0.65	1.60 to 1.70	1.650	-0.80 to -0.40	-0.60
0.80 to 1.30	1.00	1.70 to 1.75	1.725	-0.40 to -0.10	-0.25
		1.75 to 1.80	1.775	-0.10 to 0.20	0.05
		1.80 to 1.85	1.825	0.20 to 0.50	0.35
		1.85 to 1.90	1.875	0.50 to 0.80	0.65
		1.90 to 1.95	1.925	0.80 to 1.00	0.90
		1.95 to 2.00	1.975		
		2.00 to 2.10	2.050		

FIG. 3. (Color online) (a) Reconstructed mass plotted against the measured momentum. A logarithmic yield density scale is employed. The lines show the mass cuts used to identify kaon candidates. (b) Reconstructed mass for positively charged particles. The kaon peak is enhanced relative to the pion and proton peaks in the range 0.3–0.7 GeV due to the filtering condition.

are removed with a simple missing-mass cut in which the detected hadron is assumed to be a pion. The resulting hyperon missing-mass distribution over the entire kinematic range is shown in Fig. 5. Both the $\Lambda(1116)$ and $\Sigma^0(1193)$ hyperons are apparent, along with several higher mass hyperons.

D. Background corrections

To remove the multiparticle final state background channels such as $e'p\pi\pi$, the phase space background was modeled by selecting the tails of the pion and proton mass distributions. To do this, hadrons in the mass region 0.275–0.725 GeV

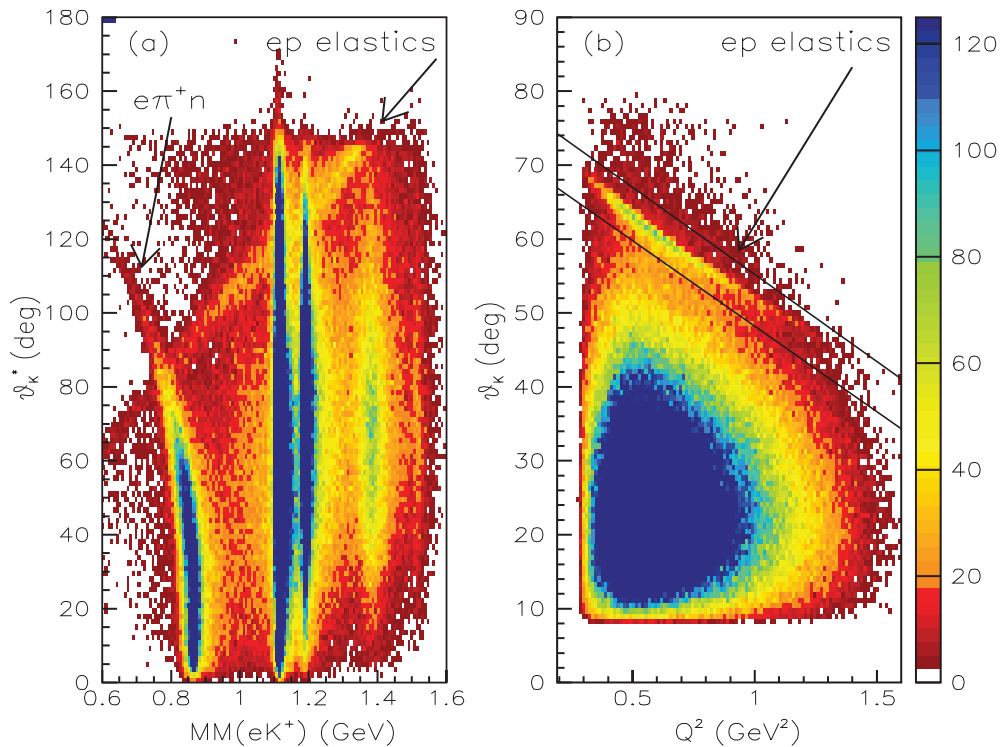FIG. 4. (Color online) (a) θ_K^* vs ^{1}H$(e, e'K^+)$ missing mass showing ep elastic events and $e'\pi^+n$ events. The vertical bands correspond to ground state $\Lambda(1116)$ and $\Sigma^0(1193)$ hyperons, and the $\Sigma^0(1385)/\Lambda(1405)$ hyperons. (b) θ_K (laboratory angle) vs Q^2 for ^{1}H$(e, e'K^+)$ events showing the ep elastic events and the cut used to remove them.
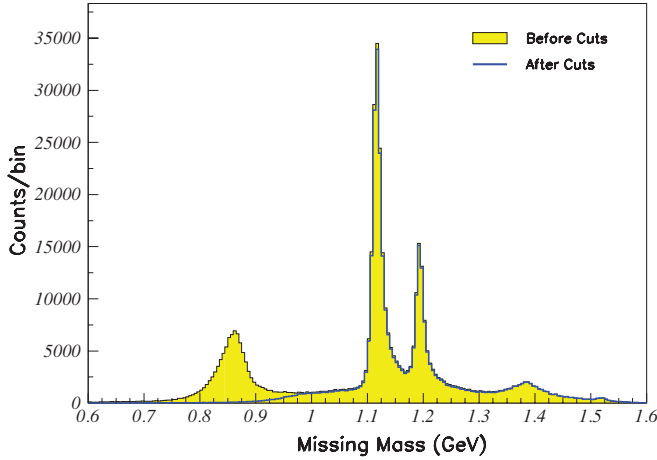
FIG. 5. (Color online) Missing mass for ^{1}H$(e, e'K^+)$ summed over the entire range of Q^2, W, $\cos\theta_K^*$, and ϕ of the data before and after removing the elastic ep events and the $e'\pi^+n$ events.

but outside the momentum-dependent kaon mass cuts were selected. Background missing-mass distributions were calculated for these particles, assigning them the kaon mass. These background distributions were fit to the ^{1}H$(e, e'K^+)$ missing-mass distribution using a maximum log likelihood method appropriate for low statistics. The fraction of each background distribution present in the data was thus estimated, and the normalized background contributions were subtracted from the data. Figure 6 shows the missing-mass distributions for two representative bins with the fitted background distributions overlaid. The Λ hyperon yields are the number of events in the background-subtracted missing-mass spectra in the mass range from 1.095 to 1.165 GeV.

E. Detector efficiency and acceptance

Geometric fiducial cuts were used to ensure that all final state charged particles were detected within the volume of CLAS where the detection efficiency is relatively large and uniform. These cuts remove the edges of the CLAS detectors and depend upon the momentum of the particles, as well as the torus magnetic field setting. The response of the CLAS detector was simulated using GSIM, a GEANT-based [42] simulation package for CLAS, that combines the geometrical configuration with the inefficiencies of the various parts of

the detector. Monte Carlo techniques were used to generate ^{1}H$(\vec{e}, e'K^+)\Lambda$ events for each helicity state of the incident electrons by including the helicity-dependent fifth structure function in the MB model [23,35].

Acceptance correction factors were obtained for each kinematic bin of Q^2, W, $\cos\theta_K^*$, and ϕ and for the two torus field settings, and the effect of the acceptance corrections on the helicity-dependent asymmetries was examined. In the limit of large statistics in the Monte Carlo simulation, the corrected asymmetries are indistinguishable from the uncorrected asymmetries. One should not expect any helicity dependence to the CLAS acceptance outside of negligible bin-migration effects. Thus, the acceptance correction was observed to cancel out (within the statistical uncertainties of both the data and Monte Carlo) in the asymmetry, and no acceptance corrections were applied to the asymmetry measurements. However, a systematic uncertainty associated with not including acceptance corrections has been estimated (see Sec. IV H).

F. Radiative corrections

Radiative corrections were performed on the extracted reaction yields using the exact calculation for the exclusive approach by Afanasev *et al.* [43]. This approach is based on the covariant procedure of infrared-divergence cancellation by Bardin and Shumeiko [44]. The exclusive approach is used to correct the cross section, in terms of not only the leptonic variables but also the hadronic variables in exclusive electroproduction. These calculations were adapted for kaon electroproduction in this work with a cross section model that included a contribution from $\sigma_{LT'}$. The radiative correction factors were the ratio of the Born and the radiative cross sections, described in terms of four kinematic variables, Q^2, W, $\cos\theta_K^*$, and ϕ. The radiative corrections are up to 30% for a given helicity state but essentially cancel out in the asymmetries.

G. Extraction of $\sigma_{LT'}$

The extraction of $\sigma_{LT'}$ requires knowledge of both the asymmetry $A_{LT'}$ and the unpolarized cross section σ_0, which
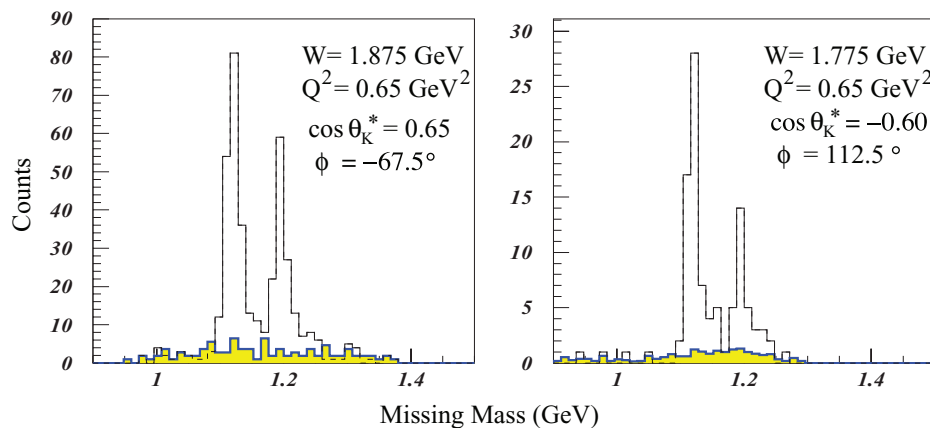

FIG. 6. (Color online) Examples of the background fit results for two typical kinematic bins with $h = +1$. The plots show the raw missing-mass plots with the fitted background (solid histogram) overlaid.

can be seen by rearranging Eq. (9) as

$$\frac{A_{LT'}\sigma_0}{\sqrt{\epsilon(1-\epsilon)}} = \sigma_{LT'}\sin\phi. \tag{11}$$

$A_{LT'}$ is determined by forming the asymmetry of the $K^+\Lambda$ yields for the positive and negative beam helicity states ($h = \pm 1$) as

$$A_{LT'} = \frac{\left(\frac{d\sigma}{d\Omega_K^*}\right)^+ - \left(\frac{d\sigma}{d\Omega_K^*}\right)^-}{\left(\frac{d\sigma}{d\Omega_K^*}\right)^+ + \left(\frac{d\sigma}{d\Omega_K^*}\right)^-} = \frac{1}{P_b}\left(\frac{N^+ - N^-}{N^+ + N^-}\right), \tag{12}$$

where $(\frac{d\sigma}{d\Omega_K^*})^\pm$ is the cross section given by Eq. (7) and $N^\pm$ corresponds to the corrected yields for the positive and negative helicity states. The electron beam is partially polarized; therefore, the measured asymmetries are also scaled by the measured beam polarization P_b.

A correction for the beam charge asymmetry (differences in the integrated beam charge for the different helicity states of the beam) is also included. This is an extremely small correction and was measured to be 2.99×10^{-3}. It was determined by measuring the helicity-dependent yield ratio for ep elastic scattering, which, outside of parity-violating effects, is exactly unity.

The unpolarized differential cross sections, σ_0, for the $^1H(\vec{e}, e'K^+)\Lambda$ reaction that are used in this work are the published CLAS results from the same data set [5]. The data from Ref. [5] were bin-centered in Q^2, W, and $\cos\theta_K^*$. In that analysis, σ_0 was measured with the same binning in the variables Q^2, W, and $\cos\theta_K^*$, and the ϕ-dependent cross sections were then used to extract the structure functions, $\sigma_U = \sigma_T + \epsilon\sigma_L$, σ_{TT}, and σ_{LT}.

To smooth out the statistical fluctuations of the unpolarized cross section data, a two-dimensional simultaneous fit in ϕ and $\cos\theta_K^*$ of the data was done. The resulting fitted ϕ- and $\cos\theta_K^*$-dependent cross sections were used in the extraction of $\sigma_{LT'}$. The measured ϕ-dependent cross section in a given bin ϕ^i is the cross section $\bar{\sigma}_0^i$ averaged over the span of the ϕ bin from ϕ_l^i to ϕ_u^i (upper and lower limits of the bin) and is given by

$$\bar{\sigma}_0^i = \frac{1}{\Delta\phi^i}\int_{\phi_l^i}^{\phi_u^i}(\sigma_U + c_+\sigma_{LT}\cos\phi + \epsilon\sigma_{TT}\cos 2\phi)\,d\phi$$

$$= \frac{1}{\Delta\phi^i}\left[\sigma_U\Delta\phi^i + c_+\sigma_{LT}\left(\sin\phi_u^i - \sin\phi_l^i\right)\right.$$

$$\left. + \frac{\epsilon}{2}\sigma_{TT}\left(\sin 2\phi_u^i - \sin 2\phi_l^i\right)\right], \tag{13}$$

where $\Delta\phi^i = \phi_u^i - \phi_l^i$ and $c_+ = \sqrt{\epsilon(1+\epsilon)}$.

In addition to the trivial ϕ dependence, the unpolarized cross section has some unknown $\cos\theta_K^*$ dependence. The separated structure functions can be described by a polynomial in $x = \cos\theta_K^*$. Using a simple comparison of χ^2/degree-of-freedom, we found that a third-order polynomial in x is entirely sufficient. The structure functions, therefore, were fit with the following forms:

$$\sigma_U = U_0 + U_1 x + U_2 x^2 + U_3 x^3, \tag{14}$$

$$c_+\sigma_{LT} = LT_0 + LT_1 x + LT_2 x^2 + LT_3 x^3, \tag{15}$$

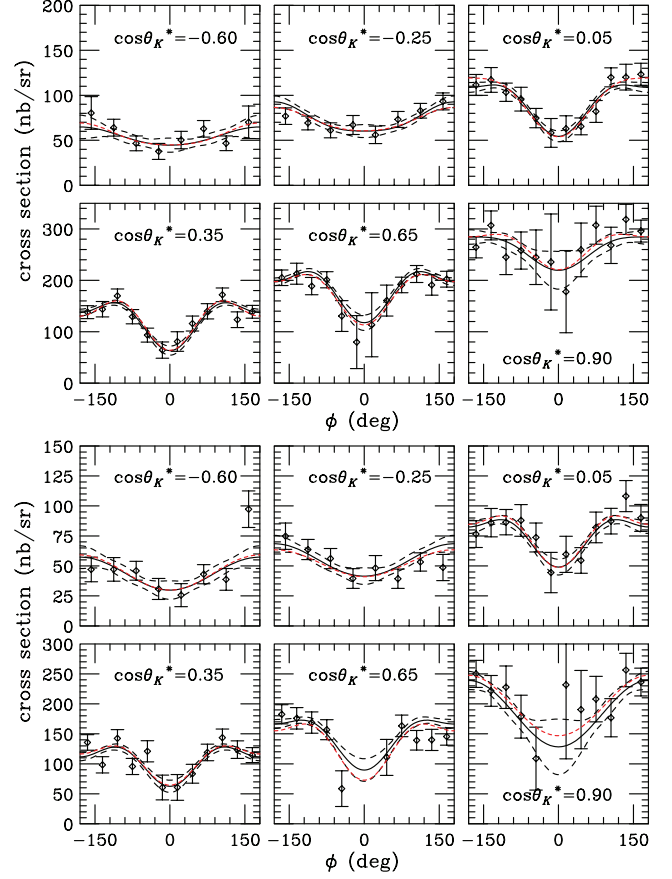$$\epsilon\sigma_{TT} = TT_0 + TT_1 x + TT_2 x^2 + TT_3 x^3. \tag{16}$$

FIG. 7. (Color online) Fits to the unpolarized cross section σ_0 vs ϕ for our six $\cos\theta_K^*$ points for $W = 1.875$ GeV and $Q^2 = 0.65$ and 1.00 GeV^2 (top and bottom panels, respectively). The data and red/light short-dashed curves are from Ref. [5]. The solid black curve in each plot is from the fit described in the text and the dashed curves represent a $\pm 1\sigma$ error band around the fit.

Samples of the resulting fits are shown in Fig. 7. In each plot, the black solid line is the best fit, and the dashed lines represent a $\pm 1\sigma$ error band extracted from the error matrix of the fit. As expected, the error band is smaller than the uncertainty of the nearby data points. This leads to a smaller contribution to the uncertainty of $\sigma_{LT'}$ than if the σ_0 data were used directly. The red/light dashed lines in the figures are from using the one-dimensional ϕ fits used in the structure function separation of Ref. [5]. The one-dimensional ϕ fits are very similar to the simultaneous $\phi/\cos\theta_K^*$ fits and usually fall within the error band, while the unpolarized structure functions also agree well with those extracted in Ref. [5]. This parametrization of the cross section is then used to determine the ϕ-dependent cross section averaged over the same bin size as each corresponding asymmetry point.

As with the cross sections, the measured asymmetries are the average values over the span of the given ϕ bins. Integrating Eq. (9) over the size of the ϕ bin results in

$$A_{LT'} = A_{LT'}^{\text{meas}}\frac{\sin\phi\Delta\phi}{\cos\phi_l - \cos\phi_u}. \tag{17}$$

The asymmetry $A_{LT'}$ has not been corrected for the finite bin size in the variables Q^2, W, and $\cos\theta_K^*$. As will be discussed in Sec. IV H, such corrections are very small compared to the uncertainties and are very sensitive to the model choice. Therefore, a systematic uncertainty associated with not making this correction was estimated.

To extract $\sigma_{LT'}$, a simple sine fit was performed according to Eq. (11), where the kinematic factor $\sqrt{\epsilon(1-\epsilon)}$ was calculated at the bin-centered value of Q^2 and W for each bin (see Table I). Samples of the data and the resulting fits are shown in Fig. 8. The solid curves are the fit result, and the dashed curves indicate the $\pm 1\sigma$ error band from the fit.

The error bars on the data points are a combination of the contributions from both $A_{LT'}$ and σ_0 and are given by

$$\delta(A_{LT'}\sigma_0) = \sqrt{(A_{LT'}\delta\sigma_0)^2 + (\sigma_0\delta A_{LT'})^2}. \qquad (18)$$

The uncertainty $\delta A_{LT'}$ is the quadrature sum of the statistical and ϕ-dependent systematic uncertainties (see Sec. IV H for details), while $\delta\sigma_0$ comes from the fit of the cross sections described above.

H. Systematic uncertainties

Various sources of systematic uncertainty that affect the measured asymmetries $A_{LT'}$ and the extracted structure functions $\sigma_{LT'}$ are considered in this analysis. The sources of systematic uncertainty that affect the measured asymmetries include uncertainties due to yield extraction, fiducial cuts, acceptance corrections, radiative corrections, and the beam charge asymmetry. These are uncorrelated point-to-point uncertainties. Scale-type uncertainties affect $\sigma_{LT'}$ only and include the bin-centering and beam polarization uncertainties, as well as the systematic uncertainties in the measurement of the unpolarized cross section σ_0. Table II summarizes the various systematic uncertainties that affect $A_{LT'}$ and $\sigma_{LT'}$.

In the case of the ϕ-dependent uncertainties, all but the yield extraction uncertainty are dominated by statistical uncertainties. The uncertainty due to the background-subtraction (yield extraction) procedure was estimated to be the same as that determined in the cross section extraction procedure [5]. In that analysis, various changes to the procedures were studied, such as changing the histogram bin size in the fitting procedure and using different forms for the background shape (e.g., using both misidentified pions and protons, only misidentified pions,
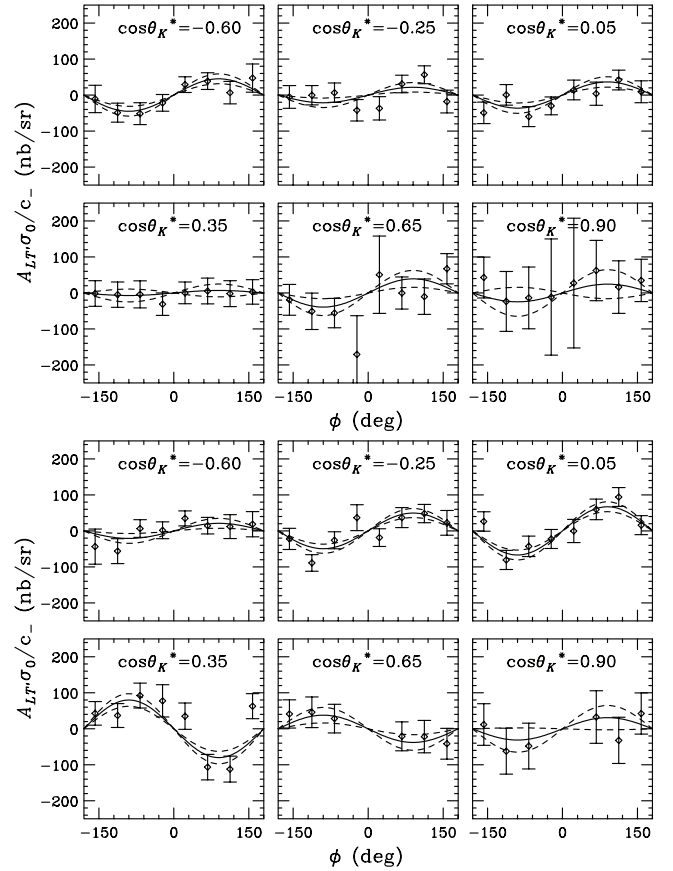

FIG. 8. Measured asymmetries multiplied by the unpolarized cross section and divided by the kinematic factor $c_- = \sqrt{\epsilon(1-\epsilon)}$ vs ϕ for our six $\cos\theta_K^*$ points for a typical kinematic bin of $W = 1.875$ GeV and $Q^2 = 0.65$ and 1.00 GeV^2 (top and bottom panels, respectively). The solid curves show the results of the $\sin\phi$ fits, and the dashed lines show the $\pm 1\sigma$ error band from the fits.

and only misidentified protons), and it was concluded that all systematic effects get larger in direct proportion to the size of the statistical uncertainty. When statistics are good (roughly 100 counts/bin), the residual systematic uncertainties are very small. It was determined that the remaining systematic uncertainty due to the yield extraction is roughly equal to 25% of the size of the statistical uncertainty in any given bin

TABLE II. Summary of the systematic uncertainties applied to $A_{LT'}$ and $\sigma_{LT'}$. The two entries for the unpolarized cross section uncertainty are for the $Q^2 = 0.65$ and 1.00 GeV^2 data sets.

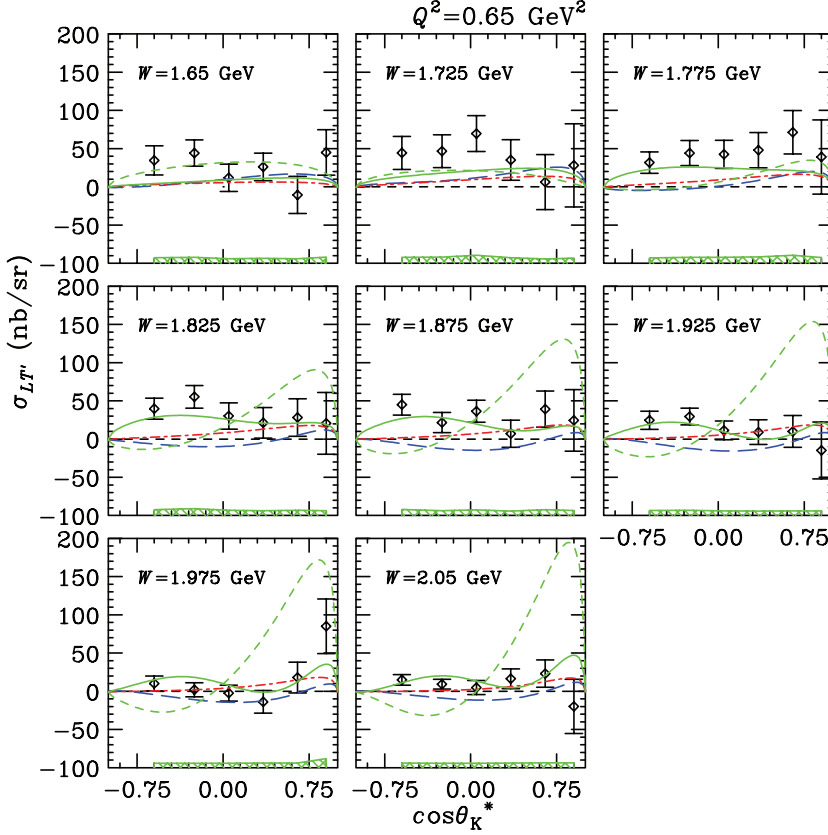| Type	Source	Systematic uncertainty $A_{LT'}$
$A_{LT'}$ (ϕ dependent)	Yield extraction method	$0.25 \times$ stat. uncertainty of yield
	Acceptance function (GSIM)	0.033
	Fiducial cuts	0.027
	Radiative corrections	0.009
	Beam charge asymmetry	1.45×10^{-4}
$\sigma_{LT'}$	Bin centering	5.8 nb/sr (absolute)
	Beam polarization	$\frac{\delta P_b}{P_b}\sigma_{LT'} = 0.023\,\sigma_{LT'}$
	Unpolarized cross section	$0.124\,\sigma_{LT'}, 0.115\,\sigma_{LT'}$

FIG. 9. (Color online) Polarized structure function $\sigma_{LT'}$ (nb/sr) vs $\cos\theta_K^*$ for $Q^2 = 0.65\,\mathrm{GeV}^2$ and W points as indicated. The curves are calculations from the MB isobar model [45] (blue long dashes), the GLV Regge model [46] (red dash-dot), the Ghent RPR model including a $D_{13}(1900)$ state [47] (green solid), and the Ghent RPR model including a $P_{11}(1900)$ state [47] (green short dashes). The shaded bars indicate the estimated overall systematic uncertainty on the results.

(defined by Q^2, W, and $\cos\theta_K^*$). This factor was determined by fitting the distributions of the yield variation when comparing the different yield extraction approaches as a function of the extracted yields. This uncertainty was added linearly to the statistical uncertainty for the helicity-dependent yields (i.e., the overall statistical uncertainty was increased on each yield by a factor of 1.25).

To estimate the uncertainties due to fiducial cuts, acceptance, and radiative corrections, the corrected or nominal asymmetries were compared with the asymmetries that resulted from using either an alternative correction or cut. The rms width of the difference between the nominal and alternative asymmetries, weighted by the statistical uncertainty of the asymmetry, was determined, and this was used as the estimate of the systematic uncertainty. For the acceptance effect, the difference between using no acceptance correction (nominal) and applying an acceptance correction was studied. This is certainly an overestimation in this case; however, the uncertainty is small compared to the other sources of systematic uncertainty and much smaller than the statistical uncertainty. For the fiducial cut uncertainty, the extent of the fiducial cuts was varied over a large range. The resulting asymmetries were compared with the nominal asymmetries. Finally, for the radiative correction uncertainty, two different physics models were used as input to the radiative correction code. The first model, from Mart and Bennhold [23], was used to obtain the nominal radiative correction factors. The second model was obtained from a parametrization of the $\sigma_{LT'}$ data. It has been implicitly assumed that the correction method is dominated by the uncertainties from the physics models.

The uncertainties for the background subtraction, fiducial cuts, acceptance, radiative corrections, and beam charge asymmetry are absolute uncertainties and were added in quadrature to the statistical uncertainty of each asymmetry data point before the extraction of $\sigma_{LT'}$.

The end result of this analysis is the extraction of the fifth structure function, $\sigma_{LT'}$, at specific points in Q^2, W, and $\cos\theta_K^*$ using Eq. (11). These kinematic points are listed in Table I (note that our bin "center" for the Q^2 bin from 0.8 to 1.3 GeV^2 was 1.00 GeV^2 as given by Ref. [5], and not the true center at $Q^2 = 1.05\,\mathrm{GeV}^2$). The beam-helicity asymmetry, however, is sorted into particular *bins* of Q^2, W, and $\cos\theta_K^*$, and thus a bin-centering correction must be considered to extract $\sigma_{LT'}$ at specific kinematic points. The bin-centering correction would be applied to the binned asymmetries as

$$A_{LT'}^{\mathrm{BC}} = A_{LT'}\left(\frac{A_{LT'}^{\mathrm{point}}}{A_{LT'}^{\mathrm{avg}}}\right)_{\mathrm{model}} = A_{LT'}(\mathrm{BC}), \qquad (19)$$

where $A_{LT'}^{\mathrm{BC}}$ represents the bin-centered beam-helicity asymmetry, and $A_{LT'}$ represents the bin-averaged asymmetry. To determine the bin-centering (BC) correction factors for this analysis, a model of the CLAS acceptance in Q^2 vs W was developed to account for the partially filled bins. The BC factors necessarily rely on a model of $A_{LT'}$, where $A_{LT'}^{\mathrm{point}}$ is the asymmetry calculated at a specific kinematic point $(Q^2, W, \cos\theta_K^*, \phi)$ and $A_{LT'}^{\mathrm{avg}}$ is the calculated bin-averaged asymmetry. The BC factors were determined using the hadrodynamic model of Mart and Bennhold [23] as a starting point. Within the framework of this model, several different
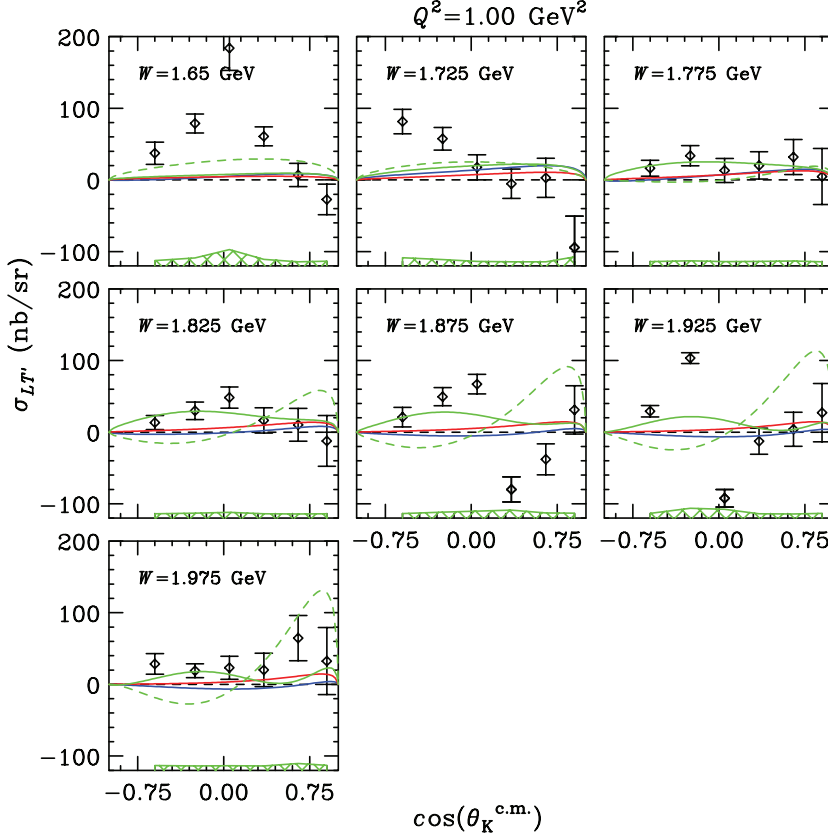
FIG. 10. (Color online) Polarized structure function $\sigma_{LT'}$ (nb/sr) vs $\cos\theta_K^*$ for $Q^2 = 1.00$ GeV^2 and W bins as indicated. The curves are as indicated in Fig. 9.

choices of elementary reaction models are available with different ingredients, such as the resonant amplitudes included, as well as the functional forms for the meson and baryon form factors, i.e., the K^+ form factor, the $K^+K^{*+}\gamma$ transition form factor, and the Λ magnetic form factor. The differences between the structure functions derived using the different models for the bin-centering corrections on the asymmetries are quite small, and none is clearly preferred by the asymmetry data. The assigned systematic uncertainty associated with the bin-centering corrections was chosen to be the largest rms width of the $\sigma_{LT'}$ differences using the different models.

The relative systematic uncertainty due to the beam polarization measurement for the data sets used in this analysis is estimated to be $\frac{\delta P}{P} = 0.023$. The estimated uncertainty on $\sigma_{LT'}$ due to the systematic uncertainty on the beam polarization is given by

$$\delta\sigma_{LT'} = |A_{LT'}^{\text{meas}}|\frac{\delta P_b}{P_b^2} = |\sigma_{LT'}|\frac{\delta P_b}{P_b}. \tag{20}$$

The resulting values of $\sigma_{LT'}$ also have an additional uncertainty associated with the systematic uncertainty in the measurement of the unpolarized cross section σ_0. The estimated systematic uncertainties for the cross sections are given in Ref. [5], which result in corresponding systematic uncertainties of $0.124\sigma_{LT'}$ and $0.115\sigma_{LT'}$ for $Q^2 = 0.65$ and 1.00 GeV^2, respectively. The quadrature sum of the uncertainties due to the bin-centering correction, beam polarization, and unpolarized cross section are shown by the shaded bars on the results (see Sec. V, Figs. 9–12).

V. RESULTS AND DISCUSSIONS

The angular dependence of $\sigma_{LT'}$ for various W points for the two Q^2 points is shown in Figs. 9 and 10, along with comparisons to several model calculations. The lower Q^2 data shown in Fig. 9 are rather flat over the full range of energy and angle, with no strong structures visible. Unlike the low Q^2 data, a strong W and angular dependence is observed in the higher Q^2 data (Fig. 10). The angular dependence shows an interesting peaking at middle angles for the lowest W point ($W = 1.65$ GeV), while a rapid sign change is seen at both $W = 1.875$ and 1.925 GeV at central angles.

The extracted $\sigma_{LT'}$ structure function results are shown as a function of W for various $\cos\theta_K^*$ points for the Q^2 points at 0.65 and 1.00 GeV^2 in the top panels of Figs. 11 and 12, respectively. For the lower Q^2 data, Fig. 11 shows that for the four backward-most kaon center-of-mass scattering angles ($\cos\theta_K^* = -0.60, -0.25, 0.05,$ and 0.35), $\sigma_{LT'}$ exhibits a smooth energy dependence with a falloff of the structure function to zero at the highest W points. In the forward kaon scattering angles, $\cos\theta_K^* = 0.65$ and 0.90, where the reaction is expected to be dominated by t-channel exchange, $\sigma_{LT'}$ is consistent with zero to within the rather large error bars of the data, and no obvious structures are present. This might indicate the dominance of a single t-channel exchange.

For the higher Q^2 data (see Fig. 12), the range of W is limited by the CLAS acceptance. Here the W dependence of $\sigma_{LT'}$ is similar to the lower Q^2 data at the more forward angles, $\cos\theta_K^* = 0.65$ and 0.90. However, there is a notable feature in the W dependence in the backward and middle kaon angles. At $\cos\theta_K^* = -0.25, 0.05$ and 0.35, the data show an interesting
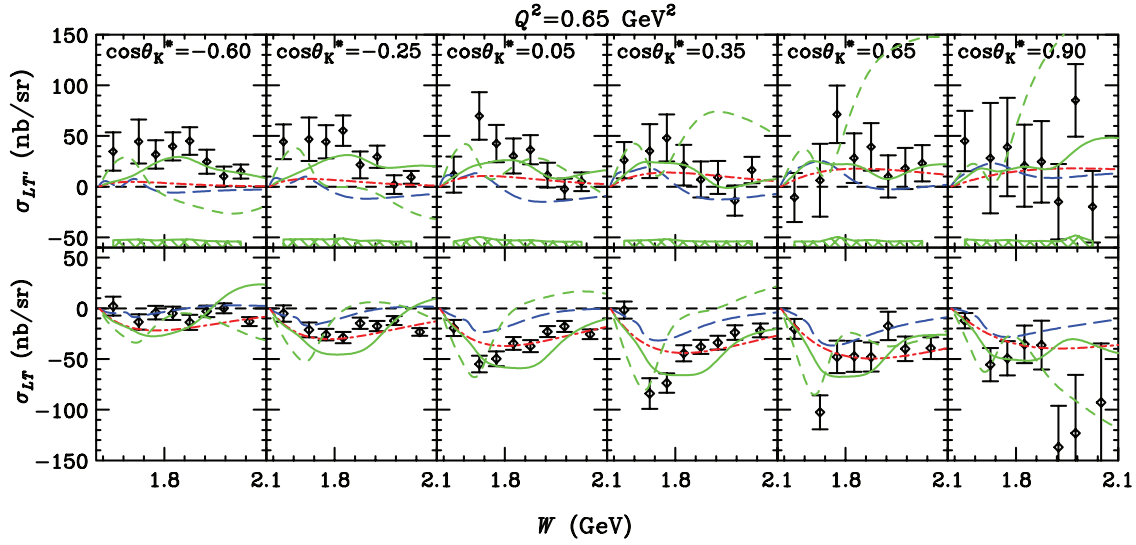
FIG. 11. (Color online) Polarized structure function $\sigma_{LT'}$ as a function of W for various $\cos\theta_K^*$ (upper panel) compared with the measured σ_{LT} from Ref. [5] (lower panel) for $Q^2 = 0.65$ GeV^2. The curves are as indicated in Fig. 9.

interference feature around 1.9 GeV, with a rapid change of sign at $\cos\theta_K^* = 0.05$ and 0.35. While at the very backward angles, $\cos\theta_K^* = -0.60$, a strong enhancement is seen at about $W = 1.7$ GeV with a flat response for higher W. For both of the Q^2 values, $\sigma_{LT'}$ goes to zero at higher W.

The results are compared with calculations from the MB isobar model [45] (blue long dashes), the GLV Regge model [46] (red dash-dot), the Ghent RPR model [47] including a $D_{13}(1900)$ state (green solid), and the Ghent RPR model [47] including a $P_{11}(1900)$ state (green short dashes). In general, none of the available models fully describes these data over the Q^2, W, and $\cos\theta_K^*$ ranges measured. The MB and GLV models underpredict the strength of $\sigma_{LT'}$, although they qualitatively follow the trends of the data. From the comparisons, the RPR model that includes the $P_{11}(1900)$ state is clearly ruled out as already indicated in Ref. [25], but the RPR model including the

$D_{13}(1900)$ state seems to best describe the data qualitatively. However, each of these models misses key features of the data. The disagreements with the isobar models (MB and RPR) may not be too surprising, as they have not been fit to these data. Therefore, the $\sigma_{LT'}$ structure function provides for additional new constraints on the model parameters.

A direct comparison of the measured polarized structure function $\sigma_{LT'}$ with σ_{LT} from Ref. [5] can reveal some interesting features of the data. This is shown in Figs. 11 and 12, which plot the polarized structure function $\sigma_{LT'}$ as a function of W for various $\cos\theta_K^*$ bins and compare it with σ_{LT} at the same kinematic points. The magnitudes of the two structure functions are comparable in both the lower and higher Q^2 data, although $\sigma_{LT'}$ has larger uncertainties. In the lower Q^2 data at the most backward kaon center-of-mass angle, $\cos\theta_K^* = -0.60$, σ_{LT} is essentially zero, while $\sigma_{LT'}$ is clearly
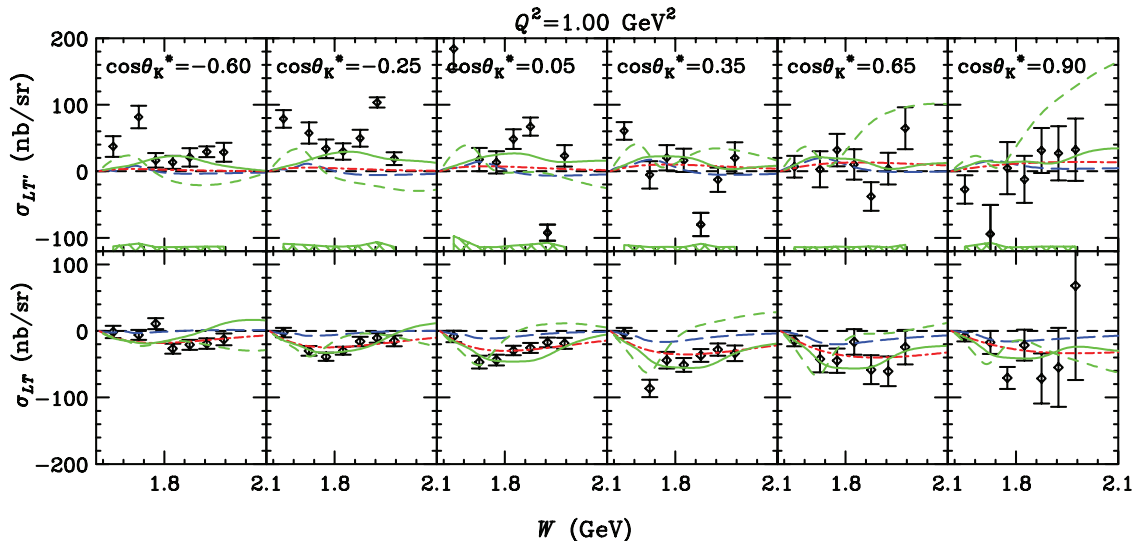

FIG. 12. (Color online) Same as Fig. 11, but for $Q^2 = 1.00$ GeV^2.

nonzero. At $\cos\theta_K^* = -0.25$, 0.05, and 0.35, σ_{LT} is similar in shape and magnitude to $\sigma_{LT'}$, but with an opposite sign. At the very forward kaon center-of-mass angles, $\cos\theta_K^* = 0.65$ and 0.90, $\sigma_{LT'}$ is consistent with zero, while σ_{LT} is nonzero. In the higher Q^2 data, and for backward and middle kaon scattering angles, $\sigma_{LT'}$ has some significant deviations from a smooth behavior, indicating significant interferences. However, the shapes of $\sigma_{LT'}$ and σ_{LT} are quite different.

All the data included in this work have been entered into the CLAS physics database [48].

VI. CONCLUSIONS

The first measurements of the structure function $\sigma_{LT'}$ for $K^+\Lambda$ electroproduction have been reported. The data span a range in W from threshold to 2.05 GeV for two Q^2 points at 0.65 and 1.00 GeV^2, and they span nearly the full center-of-mass angular range of the final state K^+. In this analysis, the energy and angular dependence of $\sigma_{LT'}$ have been investigated. $\sigma_{LT'}$ is found to be comparable on average in size to the unpolarized cross sections. The structure function is surprisingly featureless with energy and angle for the lower Q^2 data, while the higher Q^2 data indicate rather strong interference affects near threshold and at W of 1.9 GeV for central angles. $\sigma_{LT'}$ is consistent with zero at more forward angles and at higher values of W.

The data have been compared with several different model calculations. The GLV Regge calculation generally underpredicts the data. This is perhaps not too surprising given that it includes no explicit s-channel processes, which are expected to show clear signatures in $\sigma_{LT'}$. Comparisons with the MB isobar model and RPR hybrid isobar/Regge model (which did not include any CLAS electroproduction data in their fits) indicate that the model parameters need to be tuned in order to reproduce the overall average strength seen in $\sigma_{LT'}$. A bigger

challenge for these models is to explain the strong interference signatures in the data. Even though the CLAS σ_{LT} and $\sigma_{LT'}$ data have rather sizable statistical uncertainties, the data do have a good deal of discriminating power with regard to certain assumptions about which resonant states are included.

The $\sigma_{LT'}$ results were also compared with the results of the measurements for σ_{LT} [5] at the same kinematic points. While $\sigma_{LT'}$ has larger uncertainties, the magnitudes of the two structure functions are comparable. In our lower Q^2 data, $\sigma_{LT'}$ is quite smooth with W and $\cos\theta_K^*$. However, at the high Q^2 value, $\sigma_{LT'}$ shows strong interference and/or FSI signatures at middle and backward kaon scattering angles. Together, these two observables provide more complete information on the amplitudes underlying the longitudinal-transverse response for this reaction.

The question of the presence of any new resonances must wait for further work with the existing hadrodynamic models and partial wave analyses applied to the full range of the data. Fortunately, the new information presented here will impose reasonable constraints on the amplitudes used to describe electroproduction of $K^+\Lambda$ and $K^+\Sigma^0$ final states, making these models more reliable for future interpretation and prediction.

[1] R. Koniuk and N. Isgur, Phys. Rev. D **21**, 1868 (1980).

[2] S. Capstick and W. Roberts, Phys. Rev. D **47**, 1994 (1993).

[3] S. Capstick and W. Roberts, Phys. Rev. D **49**, 4570 (1994).

[4] S. Capstick and W. Roberts, Phys. Rev. D **58**, 074011 (1998).

[5] P. Ambrozewicz *et al.* (CLAS Collaboration), Phys. Rev. C **75**, 045203 (2007).

[6] G. Niculescu *et al.*, Phys. Rev. Lett. **81**, 1805 (1998).

[7] R. M. Mohring *et al.*, Phys. Rev. C **67**, 055205 (2003).

[8] D. S. Carman *et al.* (CLAS Collaboration), Phys. Rev. Lett. **90**, 131804 (2003).

[9] Brian A. Raue and Daniel S. Carman, Phys. Rev. C **71**, 065209 (2005).

[10] C. N. Brown *et al.*, Phys. Rev. Lett. **28**, 1086 (1972).

[11] C. J. Bebek *et al.*, Phys. Rev. Lett. **32**, 21 (1974).

[12] T. Azemoon *et al.*, Nucl. Phys. **B95**, 77 (1975).

[13] C. J. Bebek *et al.*, Phys. Rev. D **15**, 594 (1977); **15**, 3082 (1977).

[14] P. Brauel *et al.*, Z. Phys. C **3**, 101 (1979).

[15] M. Q. Tran *et al.*, Phys. Lett. **B445**, 20 (1998).

[16] K. H. Glander *et al.*, Eur. Phys. J. A **19**, 251 (2004).

[17] J. W. C. McNabb *et al.* (CLAS Collaboration), Phys. Rev. C **69**, 042201(R) (2004).

[18] R. Bradford *et al.* (CLAS Collaboration), Phys. Rev. C **73**, 035202 (2006).

[19] R. Bradford *et al.* (CLAS Collaboration), Phys. Rev. C **75**, 035205 (2007).

[20] R. G. T. Zegers *et al.*, Phys. Rev. Lett. **91**, 092001 (2003).

[21] M. Sumihama *et al.*, Phys. Rev. C **73**, 035214 (2006).

[22] C. Bennhold, H. Haberzettl, and T. Mart, in *Proceedings of Perspectives in Hadronic Physics,* edited by S. Boffi *et al.* (World Scientific, Singapore, 2000).

[23] T. Mart and C. Bennhold, Phys. Rev. C **61**, 012201 (1999); H. Haberzettl, C. Bennhold, T. Mart, and T. Feuster, *ibid.* **58**, R40 (1998).

[24] B. Saghai, AIP Conf. Proc. **594**, 421 (2001).

[25] T. Corthals *et al.*, Phys. Lett. **B656**, 186 (2007); T. Corthals, T. VanCauteren, J. Ryckebusch, and D. G. Ireland, Phys. Rev. C **75**, 045204 (2007).

[26] C. W. Akerlof, W. W. Ash, K. Berkelman, and C. A. Lichtenstein, Phys. Rev. **163**, 1482 (1967).

[27] G. Knochlein, D. Drechsel, and L. Tiator, Z. Phys. A **352**, 327 (1995).

[28] S. Boffi, C. Guisti, and F. D. Pacati, Phys. Rep. **226**, 1 (1993); Nucl. Phys. **A435**, 697 (1985).

[29] B. Julia-Diaz, B. Saghai, T. S. H. Lee, and F. Tabakin, Phys. Rev. C **73**, 055204 (2006).

[30] W. T. Chiang B. Saghai, F. Tabakin, and T. S. H. Lee, Phys. Rev. C **69**, 065208 (2004).

[31] V. Shklyar, H. Lenske, and U. Mosel, Phys. Rev. C **72**, 015210 (2005).

[32] T.-S. H. Lee and L. C. Smith, J. Phys. G **34**, S83 (2007).

[33] A. V. Sarantsev *et al.*, Eur. Phys. J. A **25**, 441 (2005).

[34] A. Anisovich *et al.*, Eur. Phys. J. A **24**, 111 (2005); **25**, 427 (2005).

[35] F. X. Lee, T. Mart, C. Bennhold, H. Haberzettl, and L. E. Wright, Nucl. Phys. **A695**, 237 (2001).

[36] M. Guidal, J.-M. Laget, and M. Vanderhaeghen, Nucl. Phys. **A627**, 645 (1997); Phys. Rev. C **61**, 025204 (2000); **68**, 058201 (2003).

[37] B. A. Mecking *et al.*, Nucl. Instrum. Methods A **503**, 513 (2003).

[38] M. D. Mestayer *et al.*, Nucl. Instrum. Methods A **449**, 81 (2000).

[39] E. S. Smith *et al.*, Nucl. Instrum. Methods A **432**, 265 (1999).

[40] G. Adams *et al.*, Nucl. Instrum. Methods A **465**, 414 (2001).

[41] M. Amarian *et al.*, Nucl. Instrum. Methods A **460**, 239 (2001).

[42] R. Brun *et al.*, CERN-DD-78-2-REV, 1978 (unpublished).

[43] A. Afanasev, I. Akushevich, V. Burkert, and K. Joo, Phys. Rev. D **66**, 074004 (2002).

[44] D. Y. Bardin and N. M. Shumeiko, Nucl. Phys. **B127**, 242 (1977).

[45] T. Mart, code from private communication.

[46] M. Guidal, code from private communication.

[47] T. Corthals, calculations from private communication.

[48] CLAS physics database, http://clasweb.jlab.org/physicsdb.